Article

Highly Ordered Arrays of Metal/Semiconductor Core–Shell Nanoparticles with Tunable Nanostructures and Photoluminescence

Yong Lei, and Wai-Kin Chim

J. Am. Chem. Soc., **2005**, 127 (5), 1487-1492• DOI: 10.1021/ja043969m • Publication Date (Web): 15 January 2005

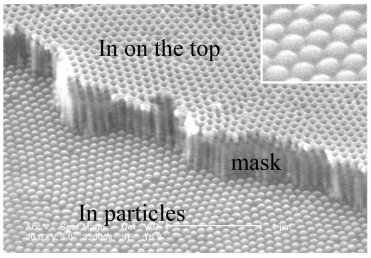

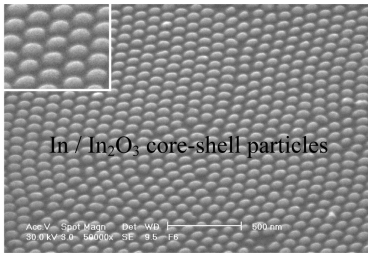

More About This Article

Additional resources and features associated with this article are available within the HTML version:

- Supporting Information
- Links to the 14 articles that cite this article, as of the time of this article download
- Access to high resolution figures
- Links to articles and content related to this article
- Copyright permission to reproduce figures and/or text from this article

View the Full Text HTML

J|A|C|S
ARTICLES
Published on Web 01/15/2005

Highly Ordered Arrays of Metal/Semiconductor Core−Shell Nanoparticles with Tunable Nanostructures and Photoluminescence

Yong Lei*,†,‡ and Wai-Kin Chim‡,§

Contribution from the Institut für Nanotechnologie, Forschungszentrum Karlsruhe, Karlsruhe, Germany 76021, and Singapore-MIT Alliance and Department of Electrical & Computer Engineering, National University of Singapore, 4 Engineering Drive 3, Singapore 117576

Received October 4, 2004; E-mail: yong.lei@int.fzk.de

Abstract: Most of the approaches so far in fabricating core−shell nanoparticles (CSNs) are based on wet-chemical methods. It is usually difficult to achieve highly ordered CSN arrays on substrates from such a wet-chemical method. In this work, highly ordered indium oxide coated indium CSNs, with a structure-dependence photoluminescence, are fabricated on Si substrates using a three-step oxidation process. By controlling the three-step oxidation process, the volume ratio of the oxide shell to the whole CSN can be adjusted continuously from 0 to 1, which results in fine-tuning of the intensity and peak-shift of the photoluminescence from the CSNs. Our work is based on a dry oxidation method for fabricating CSNs, which is capable of achieving highly ordered CSN arrays with tunable nanostructures and optical properties.

1. Introduction

Core−shell nanoparticles (CSNs) have been the subject of extensive research due to their potential application in many areas such as microelectronics, optoelectronics, catalysis, and optical devices.[1−17] CSNs with different core/shell structures have been fabricated, including semiconductor/semiconductor,[1−3] semiconductor/dielectric,[4,5] metal/metal,[6] metal/semiconductor,[7,8] metal/ carbon,[9,10] metal/dielectric,[11,12] dielectric/metal,[13,14] and nanoshells with hollow interiors.[15,16] Such composite nanoparticles have exhibited improved physical and chemical properties over their single-component counterparts, thus providing a new way to tailor the properties of the nanoparticles.[17] For the device application such as in electronic and optical areas, it is usually desirable to fabricate arrayed CSNs on substrates. In many cases, high regularity of the CSN arrays is required to obtain a precise control of their properties based on the integration of the properties of their basic component, the individual arrayed CSN. However, almost all of the approaches so far for fabricating CSNs are based on wet-chemical methods. It is usually difficult, using the wet-chemical methods, to obtain highly ordered CSN arrays on substrates with tunable structures and properties. Moreover, byproducts are inadvertently generated in many wet-chemical processes, and it is usually hard to keep the substrate surface clean when fabricating CSN arrays on substrates. All of these may limit their applications, especially in optical and electronic devices where high regularity of the CSN arrays and cleanness of the substrate surface are required.

In this work, we report the fabrication of highly ordered indium oxide (In_2O_3) coated indium (In) CSN arrays on silicon substrates using a three-step oxidation process from indium nanoparticle arrays. The latter are obtained using a recently developed skill in fabricating ordered nanoparticle arrays.[18−23] Photoluminescence (PL) spectroscopy of the CSNs shows two emission peaks with strong structure-dependence. These two

† Institut für Nanotechnologie.
‡ Singapore-MIT Alliance, National University of Singapore.
§ Department of Electrical & Computer Engineering, National University of Singapore.

(1) Kortan, A. R.; Hull, R.; Opila, R. L.; Bawendi, M. G.; Steigerwald, M. L.; Carroll, P. J.; Brus, L. E. *J. Am. Chem. Soc.* **1990**, *112*, 1327−1332.
(2) Mews, A.; Kadavanich, A. V.; Banin, U.; Alivisatos, A. P. *Phys. Rev. B* **1996**, *53*, 13242−13245.
(3) Peng, X. G.; Schlamp, M. C.; Kadavanich, A. V.; Alivisatos, A. P. *J. Am. Chem. Soc.* **1997**, *119*, 7019−7029.
(4) Spanhel, L.; Haase, M.; Weller, H.; Henglein, A. *J. Am. Chem. Soc.* **1987**, *109*, 5649−5655.
(5) Wilson, W. L.; Szajowski, P. F.; Brus, L. E. *Science* **1993**, *262*, 1242−1244.
(6) Zhou, W. L.; Carpenter, E. E.; Lin, J.; Kumbhar, A.; Slims, J.; O'Connor, C. J. *Eur. Phys. J. D* **2001**, *16*, 289−292.
(7) Averitt, R. D.; Sarkar, D.; Halas, N. J. *Phys. Rev. Lett.* **1997**, *78*, 4217−4220.
(8) Yang, Y.; Nogami, M.; Shi, J. L.; Chen, H. R.; Liu, Y.; Qian, S. X. *J. Mater. Chem.* **2003**, *13*, 3026−3032.
(9) Kim, M.; Sohn, K.; Na, H. B.; Hyeon, T. *Nano Lett.* **2002**, *2*, 1383−1387.
(10) Nikitenko, S. I.; Koltypin, Y.; Felner, I.; Shames, A. I.; Jiang, J. Z.; Markovich, V.; Gorodetsky, G.; Gedanken, A. *J. Phys. Chem. B* **2004**, *108*, 7620−7626.
(11) Lu, Y.; Yin, Y. D.; Li, Z. Y.; Xia, Y. N. *Nano Lett.* **2002**, *2*, 785−788.
(12) Aoki, K.; Chen, J. Y.; Yang, N. J.; Nagasawa, H. *Langmuir* **2003**, *19*, 9904−9909.
(13) Oldenburg, S. J.; Averitt, R. D.; Westcott, S. L.; Halas, N. J. *Chem. Phys. Lett.* **1998**, *288*, 243−247.
(14) Graf, C.; van Blaaderen, A. *Langmuir* **2002**, *18*, 524−534.
(15) Sun, Y. G.; Xia, Y. N. *Anal. Chem.* **2002**, *74*, 5297−5305.
(16) Hao, E. C.; Li, S. Y.; Bailey, R. C.; Zou, S. L.; Schatz, G. C.; Hupp, J. T. *J. Phys. Chem.* **2004**, *108*, 1224−1229.
(17) Caruso, F. *Adv. Mater.* **2001**, *13*, 11.
(18) Masuda, H.; Satoh, M. *Jpn. J. Appl. Phys.* **1996**, *35*, L126−L129.
(19) Masuda, H.; Yasui, K.; Nishio, K. *Adv. Mater.* **2000**, *12*, 1031.
(20) Cheng, G.; Moskovits, M. *Adv. Mater.* **2002**, *14*, 1567.
(21) Sander, M. S.; Tan, L. S. *Adv. Funct. Mater.* **2003**, *13*, 393−397.
(22) Lei, Y.; Yeong, K. S.; Thong, J. T. L.; Chim, W. K. *Chem. Mater.* **2004**, *16*, 2757−2761.
(23) Chen, Z.; Lei, Y.; Chew, H. G.; Teo, L. W.; Choi, W. K.; Chim, W. K. *J. Cryst. Growth* **2004**, *268*, 560−563.

peaks are located at wavelengths of about 326−339 and 476 nm, which are attributed to the In_2O_3 band gap and oxygen vacancy emission, respectively. By controlling the three-step oxidation process, we can adjust the volume ratio of the oxide shell to the whole CSN continuously from 0 to 1, which results in fine-tuning of the PL characteristics of the In/In_2O_3 CSNs, such as the PL intensity and peak-shift. Our method in fabricating large-scale semiconductor-coated metal CSN arrays on substrates is based on a dry oxidation process, which provides a new selection in fabricating CSNs other than the wet-chemical methods. In addition, as a well-known transparent conducting oxide, In_2O_3 has some structure-related optical and optoelectronic properties and has been widely used in solar cells,[24] flat-panel displays,[25] architectural glasses,[26] organic light-emitting diodes,[27] and ultrasensitive toxic-gas detectors.[28] The tunable core−shell nanostructures of the ordered CSN arrays in this paper are expected to have some tunable properties other than PL.

2. Experimental Section

Figure 1 outlines the fabrication processes.

Chemicals. Oxalic acid dihydrate ($C_2H_2O_4·2H_2O$), *ortho*-phosphoric acid (H_3PO_4, 85%), sulfuric acid (H_2SO_4, 95−97%), perchloric acid ($HClO_4$, 70−72%), chromium(VI) oxide (CrO_3), tin(II) chloride dehydrate ($SnCl_2·2H_2O$), acetone (99.5+%), and ethanol (99.8+%) were purchased from Merck. 6% PMMA/chlorobenzene solution (950 PMMA C6) was purchased from Microlithography chemical (Newton, MA).

Fabrication of Ultrathin Alumina Masks (UTAMs) and In Nanoparticle Arrays on Si/SiO_2 Substrates (Details in Supporting Information, Methods). First is the preparation of an UTAM on the surface of the substrate (Figure 1a). A typical UTAM on a silicon (Si) wafer is shown in Figure 1a′. The high pore regularity arises from a long first anodization duration of 10 h. After the deposition of In (Figure 1b), the UTAM is removed, leaving a highly ordered In nanoparticle array on the substrate. Figure 1b′ shows this array on a Si wafer, where part of the UTAM is left behind intentionally. The diameter distribution of the nanoparticle arrays is highly monodisperse; the mean size can be adjusted from about 10 to 100 nm. The findings so far agree with the results of previous work on Ni nanoparticle arrays.[22]

Fabrication of In/In_2O_3 CSN Arrays. The oxidation of the In nanoparticles is the decisive step to obtain In/In_2O_3 CSNs. It is known that, for low melting-point metals such as In, a normal oxidation process with a relatively fast temperature increment will cause the granulation of the metal film or the agglomeration of the metal nanoparticles.[29−32] In our case of densely arrayed nanoparticles on substrates, neighboring molten In particles will migrate along the surface and agglomerate into large blocks of In. All of these will destroy the regularity of the nanoparticles. Here, we used a three-step oxidation process to realize the transformation of In nanoparticles to In/In_2O_3 CSNs and In_2O_3 nanoparticles (see Figure 2 for the heating curve). The first step is the preheating process. The temperature was increased very fast to 146 °C, which is around the melting point of the In nanoparticles [for In nanoparticles with sizes of about several tens of nanometers, the melting point is about 10 °C lower than the melting point of bulk In (156.61 °C)],[33] and held for 1 h. In the second step, the temperature ramp

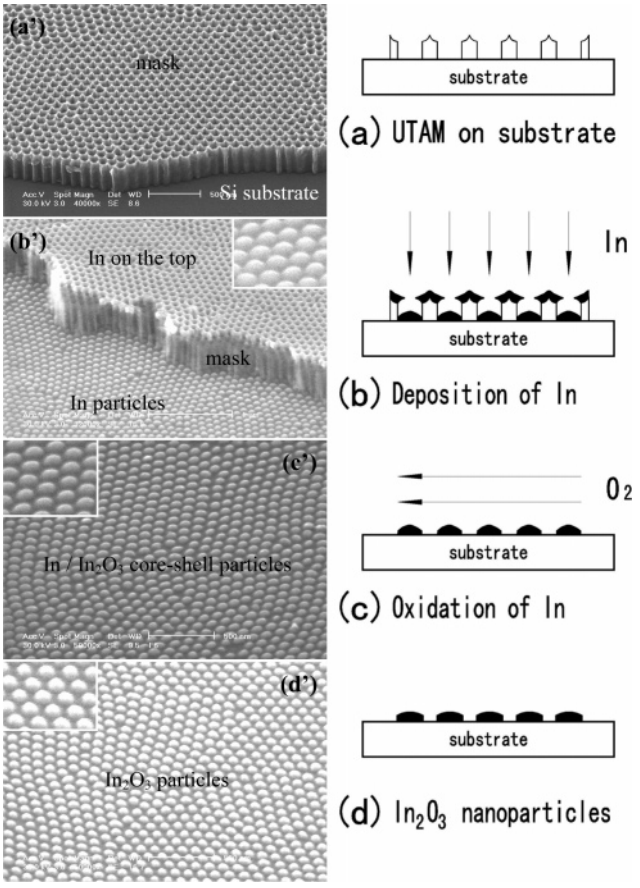

Figure 1. Schematic outline of the fabrication process. (a′), (b′), (c′), and (d′) are SEM images of the products in procedures (a), (b), (c), and (d), respectively. (a′) shows an UTAM on Si substrate; pore diameter, cell size, and thickness of the UTAM are about 75, 105, and 350 nm, respectively. (b′) shows the initial In nanoparticle arrays, with part of the UTAM remaining. (c′) shows In/In_2O_3 CSN arrays after the temperature ramp process. (d′) shows the final In_2O_3 nanoparticle arrays. The insets in (b′), (c′), and (d′) are the enlarged images. The average particle diameters in (b′), (c′), and (d′) are about 70, 70−75, and 75 nm, respectively.

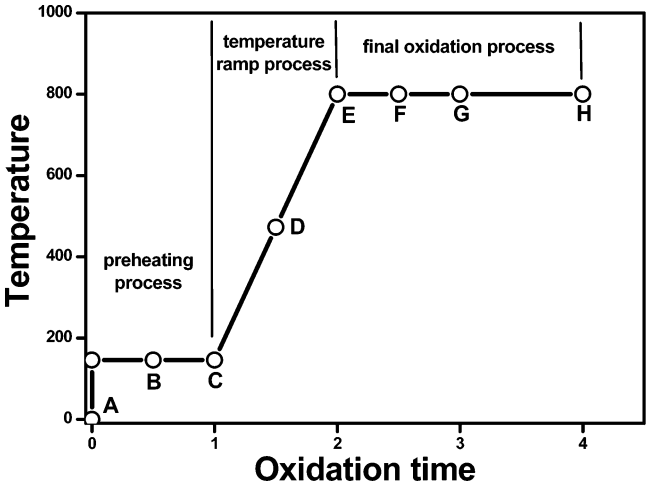

Figure 2. Heating curve of the three-step oxidation process in which the stop-positions of eight samples (samples A−H) are clearly marked. The average diameters of the nanoparticles in samples A−H are about 45−48 nm.

(24) Hara, K.; Sayama, K.; Arakawa, H. *Sol. Energy Mater. Sol. Cells* **2000**, *62*, 441−447.
(25) Aoshima, Y.; Miyazaki, M.; Sato, K.; Akao, Y.; Takaki, S.; Adachi, K. *Jpn. J. Appl. Phys., Part 1* **2000**, *39*, 4884−4889.
(26) Grivas, C.; Mailis, S.; Eason, R. W.; Tzamali, E.; Vainos, N. A. *Appl. Phys. A* **2002**, *74*, 457−465.
(27) Kim, H.; Horwitz, J. S.; Kushto, G. P.; Qadri, S. B.; Kafafi, Z. H.; Chrisey, D. B. *Appl. Phys. Lett.* **2001**, *78*, 1050−1052.
(28) Liess, M. *Thin Solid Films* **2002**, *410*, 183−187.
(29) Kolluri, S. V.; Chandorkar, A. N. *Thin Solid Films* **1993**, *230*, 39.
(30) Lee, M. S.; Choi, W. C.; Kim, E. K.; Kim, C. K.; Min, S. K. *Thin Solid Films* **1996**, *279*, 1−3.
(31) Parent, P.; Dexpert, H.; Tourillon, G.; Grimal, J. M. *J. Electrochem. Soc.* **1992**, *139*, 276−281.
(32) Soulantica, K.; Erades, L.; Sauvan, M.; Senocq, F.; Maisonnat, A.; Chaudret, A. *Adv. Funct. Mater.* **2003**, *13*, 553−557.

process, the temperature was ramped to 800 °C at a rate of about 10 °C min^{-1}. This process took about 1 h. The third step is the final oxidation process, in which the temperature was held at 800 °C for 2 h to complete the oxidation. The whole process, including the initial heating to 146 °C, was performed in a tube furnace with a constant flow of oxygen at atmospheric pressure.

Figure 1c′ and 1d′ shows the oxidized nanoparticle arrays after the preheating process and the final oxidation process, respectively. It can be seen that there is no obvious change of the nanoparticle arrays in the three-step oxidation process:[34] the monodisperse nanoparticles are still arrayed on the substrate with high regularity. In particular, there is no agglomeration of the nanoparticles after oxidation.

Samples. A set of eight samples was used to analyze the structural changes and PL properties of the nanoparticles in the three-step oxidation process. The samples are similar samples, with identical initial In nanoparticles (average diameters of 45 nm), and the same sample area (2.25 cm^2) so as to compare the PL intensities. However, the oxidation durations of these samples are different. The stop-positions of the eight samples (denoted as samples A−H) in the three-step oxidation process are (marked in Figure 2): 0 min (A), 30 min (B), and 60 min (C) in the preheating process; 30 min (D) and 60 min (E) in the temperature ramp process; and 30 min (F), 60 min (G), and 120 min (H) in the final oxidation process. Sample A is the initial nanoparticles. Samples C, E, and H are the oxidized nanoparticles after the preheating process, the temperature ramp process, and the final oxidation process, respectively. After oxidation, all samples were cooled in the tube furnace with a constant flow of nitrogen to avoid further oxidation.

Characterization. The SEM images in this paper were obtained using a field-emission scanning electron microscope [Philips XL-30 FEG]. X-ray diffraction patterns were captured by a General Area Detector Diffraction System (GADDS), which was equipped with a high sensitive area detector (HI-STAR) that is especially suitable for those samples with texture, large grain size, and small quantity. HRTEM measurements were carried out on the CM300FEG instrument (with a 300 kV high voltage and field emission gun) and a JEOL3010 instrument (with a 300 kV high voltage). PL spectra were obtained using a RF-5301 PC fluorometer.

3. Results and Discussion

Microstructure Analyses. Figure 3 shows the microstructures of the nanoparticles in samples A, C, and H. The substrates are n-type (001) Si covered with a 2 nm thick SiO_2 layer. Cross-sectional high-resolution transmission electron microscopy (HRTEM) (a_1, b_1, and c_1) and X-ray diffraction (XRD) measurement (a_4, b_3, and c_4) were used to characterize the microstructures of the nanoparticles.

XRD measurement (Figure $3a_4$) of sample A indicates that the as-evaporated nanoparticles are In [tetragonal, *I*4/*mmm*(139)] with a (101) preferred orientation. The cross-sectional HRTEM image of an In nanoparticle (Figure $3a_1$) shows that the lattice directions are almost the same in each part of the particle, indicating its single-crystal nature. However, some lattice intensity distributions suggest the presence of regions with slight misorientations giving rise to a Moiré-like pattern. The highly crystalline nature of the In nanoparticles is also shown in Figure $3a_2$ and $3a_3$, which are the Fourier transformation image and Fourier filtered lattice image of the squared area *S* in Figure $3a_1$. The white parallel lines in Figure $3a_3$ indicate two In (101) planes, and the lattice distance agrees with the standard value of 0.271 nm. We found that the In nanoparticles are orientated with the (101) planes approximately parallel to the surface of the Si substrate, which is in agreement with the XRD results.

Figure $3b_1$ is the cross-sectional HRTEM image of a nanoparticle in sample C. We found that, at this stage, the particles are oxide-coated metal core−shell nanoparticles. XRD measurement (Figure $3b_3$) confirms that the particle is composed of In and In_2O_3 [cubic, *Ia*3(206)]. The outer shell is In_2O_3, as confirmed by the lattice distance measurement in Figure $3b_2$, and is a natural result of the oxidation of a metal particle. The thickness of the oxide shell is about 5−6 nm; thus the average growth rate of the oxide shell in the preheating process is about 5−6 nm/h and the volume ratio of the oxide shell to the whole nanoparticle is about 1/2. It is clearly that, at the beginning of the preheating process, an oxide shell is formed at the surface of the In nanoparticles. As the oxidation progresses, the inner In reacts with the oxygen at the core−shell interface, thus thickening the shell gradually. There are two possible oxygen sources in this oxidation process: the oxygen in the air around the particles and the oxygen in the SiO_2 underlayer. As shown in Figure $3b_1$, the continuous shell is located on the surfaces exposed to the oxygen, and there is no continuous shell at the bottom of the inner In core on the SiO_2 surface. This implies that there is almost no oxidation at the In interface between the In and SiO_2 underlayer.

XRD measurement (Figure $3c_4$) of sample H confirms that the In/In_2O_3 CSNs have been completely converted to In_2O_3 nanoparticles. The lattice directions are the same in each part of the particle (Figure $3c_1$) and there are no visible defects, indicating that the In_2O_3 nanoparticles are single-crystal nanoparticles. This can also be seen in the Fourier transformation pattern and the Fourier filtered lattice image of the squared area *S* in Figure $3c_2$ and $3c_3$. The white parallel lines in Figure $3c_3$ indicate two In_2O_3 (222) planes, and the lattice distance agrees with the standard value of 0.292 nm. The In_2O_3 nanoparticles are also orientated with the (222) planes parallel to the surface of the Si substrate. It has been reported that thermally evaporated In films, and consequently oxidized In_2O_3 films, on substrates such as SiO_2/Si and glass showed a (101) preferred orientation for In and a (111) preferred orientation for In_2O_3 as a natural result of the In thermal evaporation process[29−31] (see Supporting Information, detailed analyses of the crystalline orientation of the In and In_2O_3 nanoparticles).

It is clear that, after the three-step oxidation process, the particles are converted from In nanoparticles to In/In_2O_3 CSNs, and finally to In_2O_3 nanoparticles. To further study the nanostructures of the CSNs, we performed the HRTEM measurement (Figure 4) to a nanoparticle in sample E. In contrast to the previous sample, we used a substrate with a thicker SiO_2 interlayer (about 20 nm thickness) to study the influence of the SiO_2 on the oxidation. It is found, after the 1 h temperature ramp process, the oxide shell becomes much thicker with about 16 nm thickness. Thus, the average growth rate of the oxide shell in the temperature ramp process is about 10−11 nm/h, which is about twice that in the preheating process. The volume ratio of the shell to the entire CSN increases from about 1/2 in sample C to about 24/25 here. Moreover, there is no shell at the bottom of the In core, confirming that there is no oxidation at the In/SiO_2 interface.

(33) Zayed, M. K.; Hegazy, M. S.; Elsayed-Ali, H. E. *Thin Solid Films* **2004**, *449*, 254−263.

(34) Because the calculated volume ratio of In_2O_3 [tetragonal, *I*4/*mmm*(139)] to In [cubic, *Ia*3(206)] is 1.230, the extension ratio in one dimension is only about 0.071 [$(0.071 + 1)^3 = 1.230$]. Therefore, in the SEM images, there is no visible change of the size of the nanoparticles after the oxidation.

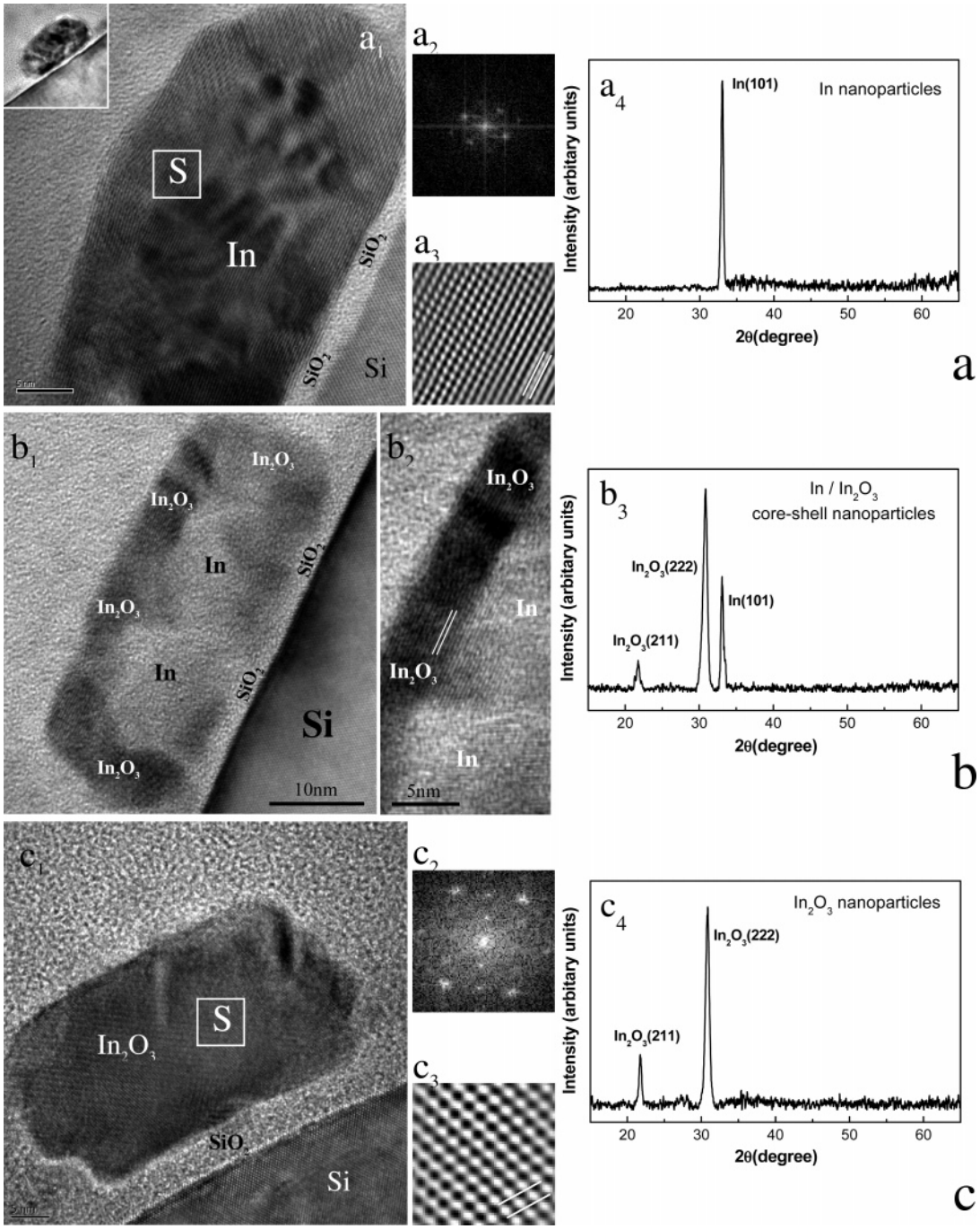

Figure 3. Microstructures of (a) In nanoparticles (sample A), (b) In/In_2O_3 core−shell nanoparticles (sample C), and (c) In_2O_3 nanoparticles (sample H). a_1, b_1, and c_1 are the cross-sectional HRTEM images of particles on the surface of SiO_2/Si. a_2, a_3 and c_2, c_3 are the Fourier transformation patterns and the Fourier filtered lattice images of the squared areas *S* in a_1 and c_1, respectively. The white parallels in a_3 and c_3 indicate the In (101) [tetragonal, *I*4/*mmm*(139)] and In_2O_3 (222) planes [cubic, *Ia*3(206)], respectively, while the lattice distances agree with the standard value of 0.271 and 0.292 nm. a_4, b_3, and c_4 are the corresponding XRD spectra. The inset in a_1 is a low-magnification image of the In nanoparticle in a_1. The thickness of the In_2O_3 shell in b_1 is about 5−6 nm. The volume ratio of the In_2O_3 shell to the whole CSN is about 1/2. b_2 is an enlarged image of an area at the surface of the nanoparticle in b_1, which clearly shows the In/In_2O_3 core−shell structure. The white parallels in b_2 in the shell indicate the In_2O_3 (222) planes with a lattice distance of about 0.290 nm.

Growth Mechanism of the In/In_2O_3 CSNs. At the beginning of the oxidation, there is a quite thin oxide shell formed on the surface of the In nanoparticle. In the preheating process, the partially melted inner In core (146 °C is around the melting point of the In nanoparticle)[33] is oxidized at the core−shell interface by the diffused oxygen from the outer surface of the shell. Because the temperature is just around the melting point of In, the growth rate of the oxide shell is quite small, about 5−6 nm/h. This slowly formed shell is extremely crucial to the formation of the stable In/In_2O_3 CSNs from In nanoparticles. For the conventional single-step oxidation process, it is usually impossible to form a stable shell at the surface because the melted In will "bump into" and break any new-formed oxide shell. In our case, after the preheating process, a relatively thick and stable oxide shell has been formed before the sample undergoes subsequent higher temperature steps. In the following temperature ramp and final oxidation process, the melted inner In core will be further oxidized, with a much higher transforma-

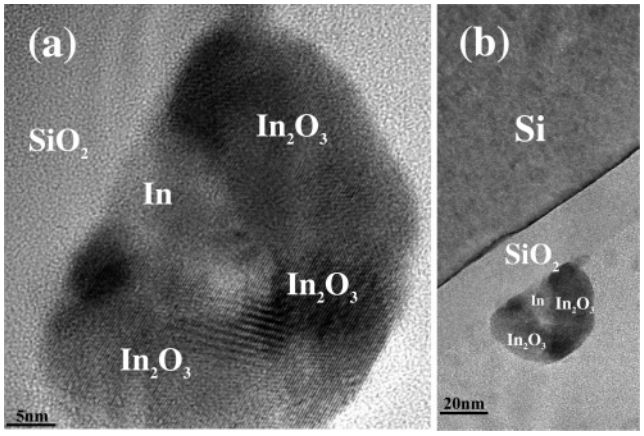

Figure 4. Core−shell structure of a CSN in sample E (a). (b) is the low magnification image which clearly shows the Si substrate with a 20 nm-thickness SiO_2 layer. The average thickness of the In_2O_3 shell is about 16 nm. The inner In core is quite small. The volume ratio of the In core to the whole CSN is about 1:25.

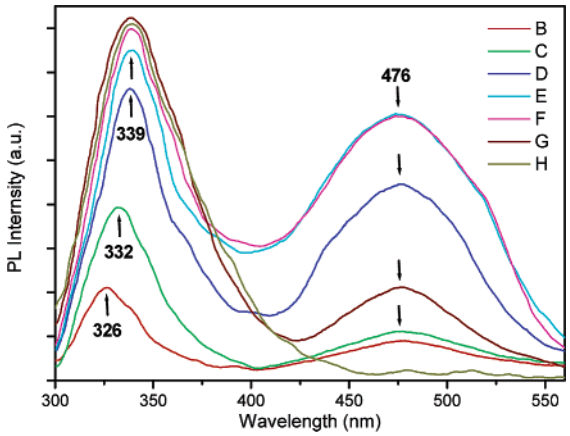

Figure 5. Room-temperature PL spectra of samples B−H. The excitation wavelength is 290 nm.

tion rate of about 10−11 nm/h, at the core−shell interface until a single-crystal In_2O_3 particle is formed.

PL Properties and Analyses. We carried out the PL measurement of the eight samples (A−H) to further analyze the structural transition of the nanoparticles in the three-step oxidation process. The PL spectra of samples B−H are shown in Figure 5. The PL spectrum of sample A is not shown because it has no visible PL peaks. In the preheating process, after sample A is oxidized for 30 min and changes to sample B, two PL peaks appear. The first PL peak is located in the ultraviolet region at a wavelength of 326 nm (denoted as band 1), and the other is a relatively weak and broad spectrum in the blue-green region which is peaked at 476 nm (denoted as band 2). When the sample is further oxidized for 30 min and changes to sample C, the PL intensity of the band 1 increases to about twice that of sample B while the peak slightly red-shifts to 332 nm. Meanwhile, there is only a slight intensity increment of band 2, which is still peaked at 476 nm. Because there is no PL for In nanoparticles, these two PL spectra should originate from the In_2O_3 shells or the core−shell interface. It has been reported that In_2O_3 nanoparticles have a strong band-gap PL emission which is peaked at 325−338 nm.[35,36] Moreover, PL emissions due to oxygen vacancies (OVs) have also been reported in In_2O_3 nanowires and nanoparticles with PL spectra peaked at 465−470,[37,38] 545,[39] and 637 nm.[30] In our case, the wavelength positions of bands 1 (326−332 nm) and 2 (476 nm) are close to the reported peaks of the band gap[35,36] and OV emission.[37,38] Thus, it is reasonable to attribute bands 1 and 2 to the band gap and OV emission, respectively. It is known that the PL intensity of the band-gap emission is proportional to the volume of the luminescent materials. Because the PL intensity of band 1 from sample B is about half of that from sample C, the shell thickness of sample B is estimated to be about 2−3 nm (refer to 5−6 nm in sample C). As mentioned above, oxygen needs to diffuse across the shell to attend the oxidation at the core−shell interface. This may lead to an insufficient oxygen supply in the oxidation process, which results in the generation of OVs in the oxide shell, especially at the core−shell interface area.

In the temperature ramp process (C−D−E), the PL peak of band 1 further red-shifts to 339 nm, and the PL intensity further increases with an increment that is approximately proportional to the volume increment of the oxide shell. The volume ratio of the shell to the whole CSN increases from about 1/2 in sample C to about 24/25 in sample E. We estimated that, on the basis of the PL intensity of band 1, the volume ratio of sample D is about 7/8, which gives an estimated shell thickness of about 12 nm. The blue-shifts of the band 1 of samples B and C, as compared to the normal band-gap emission of In_2O_3 peaked at 338 nm,[35] should arise from the quantum-sized shell thickness of about 2−3 and 5−6 nm.[35,36] As the shell thickness is much larger than the exciton Bohr diameter of In_2O_3 (in the range between 2.6 and 5 nm)[35,36] such as in samples D and E, the PL peak of band 1 remains approximately constant at a wavelength of 339 nm. The intensity of band 2 increases very fast from sample C to D and E. As mentioned above, the growth rate of the oxide shell in the temperature ramp process is much larger than that in the preheating process. This may largely increase the number of the OVs. Moreover, with the thickening of the shell, it is more difficult for the oxygen to pass through the thicker shell and reach the core−shell interface, which is the reaction site of the oxidation. This should also favor the increasing of the OVs. It is more likely that most of the OVs are distributed in an oxide layer near the core−shell interface rather than just being located at the interface. This will be verified by the PL analyses of samples F−H below.

In the final oxidation process, the PL intensity of band 1 shows a relatively small increment from samples E to F, and there is almost no intensity increment from samples F to G and H. This implies that the In core has been completely converted to In_2O_3 for sample F, indicating that samples F, G, and H are all In_2O_3 nanoparticles. However, when the In core has just disappeared (sample F), the PL intensity of the OV emission is still quite large (almost the same as that of sample E). This indicates that there are still many OVs in this newly formed In_2O_3 nanoparticles. Most of the OVs should be located in the center-bottom part of the particles, which is near the disappeared core−shell interface. This confirms that, for the CSNs in samples B−E, the OVs should be distributed in an oxide layer near the

(35) Murali, A.; Barve, A.; Leppert, V. J.; Risbud, S. H.; Kennedy, I. M.; Lee, H. W. H. *Nano Lett.* **2001**, *1*, 287−289.
(36) Seo, W. S.; Jo, H. H.; Lee, K.; Park J. T. *Adv. Mater.* **2003**, *15*, 795.
(37) Liang, C. H.; Meng, G. W.; Lei, Y.; Phillipp, F.; Zhang, L. D. *Adv. Mater.* **2001**, *13*, 1330.
(38) Zheng, M. J.; Zhang, L. D.; Li, G. H.; Zhang, X. Y.; Wang, X. F. *Appl. Phys. Lett.* **2001**, *79*, 839−841.
(39) Zhou, H. J.; Cai, W. J.; Zhang, L. D. *Appl. Phys. Lett.* **1999**, *75*, 495−49.

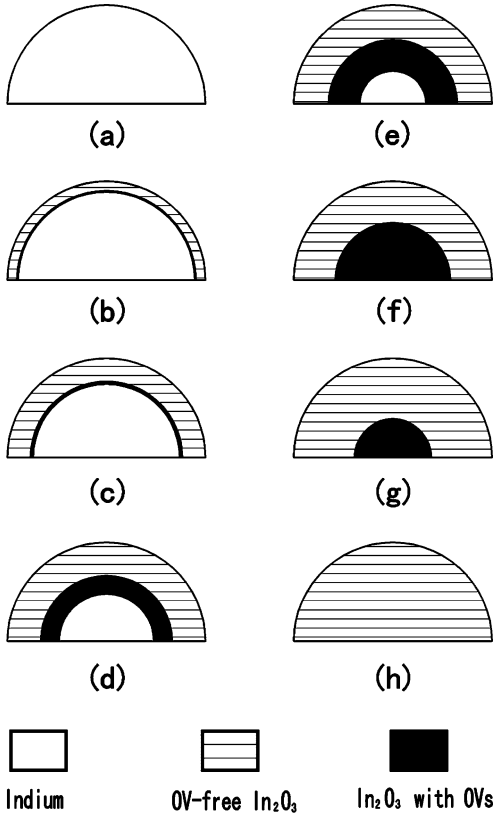

Figure 6. Schematic outline of the transition from In nanoparticles (a), to In/In_2O_3 core−shell nanoparticles (b−e), and In nanoparticles (f−h), which correspond to samples A−H (with average diameters of about 45−48 nm). The thicknesses of the In_2O_3 shells are about 2−3 (b), 5−6 (c), 12 (d), and 16 nm (e), which indicate that the volume ratios of the In_2O_3 shell to the whole CSN are about 1/4, 1/2, 7/8, and 24/25, respectively.

core−shell interface rather than just located at the interface because the OVs are not apparently decreased with the disappearance of the core−shell interface (sample F). With further oxidation from samples F to G, the PL intensity of band 2 decreases very fast. Finally, band 2 disappears for sample H. In this period, the OV sites are occupied by the oxygen diffused from the outside, resulting in the annihilation of the OVs. Actually, in the previous oxidation periods, not all of the oxygen reacts with the In core; some of them occupy the OV sites and cause the annihilation of these OVs. However, the generation of the OVs is much faster than the annihilation, resulting in the increment of the OVs. In the final oxidation process after sample F, because the In core is no longer present, all of the oxygen diffused into the particle will occupy the OV sites, thus leading to a fast OV annihilation.

Discussion. Figure 6 is the schematic outline of the transition from In nanoparticles (a) to In/In_2O_3 CSNs (b−e) and In_2O_3 nanoparticles (f−h). During the preheating process (a−b−c), the shell thickness increases from 0 to about 2−3 nm and 5−6 nm, while the volume ratio of the In_2O_3 shell to the whole CSN increases from 0 to about 1/4 and 1/2. Some OVs are generated in a thin oxide layer in the shell near the core−shell interface. During the temperature ramp process (c−d−e), the shell thickness further increases to about 12 and 16 nm while the volume ratio of the In_2O_3 shell further increases to about 7/8 and 24/25. Due to the fast oxidation, many OVs were generated and located in a relatively wide oxide layer in the shell near the interface. In the final oxidation process (e−h), the In core disappears, resulting in In_2O_3 nanoparticles. The number of the OVs decreases very rapidly and finally causes the annihilation of the OVs.

The PL of the nanoparticles is closely related to their nanostructures and the oxidation process. The PL spectrum peaked at about 326−339 nm originates from the In_2O_3 band-gap emission. Its intensity, as well as the peak-shift, is determined by the volume ratio of the shell to the whole CSN. The PL spectrum peaked at about 476 nm is attributed to the OV emission, and its intensity is changed with the oxidation process. Because the volume ratio of the shell to the nanoparticle can be adjusted continuously from 0 to 1 with the progress of the three-step oxidation process, it is practically feasible to obtain a fine-tuning of the PL from the CSNs.

It is worth noting that, using different electrolytes and anodization voltages, the pore diameters of the UTAMs can be adjusted from about 10 to 100 nm to yield In nanoparticles of corresponding size.[22] Thus, the mean size of consequently In/In_2O_3 CSNs can also be adjusted in a similar range.

4. Outlook

The work reported here, highly ordered CSN arrays on Si substrates prepared by a physical dry-oxidation approach, signifies that CSNs can be fabricated using techniques other than wet-chemical methods. The tunable PL property makes the highly ordered In/In_2O_3 CSN arrays quite suitable to be used as optical devices. Moreover, the three-step oxidation process can be applied more generally to other metals in fabricating highly ordered metal/oxide CSN arrays. Work for Sn, Zn, and Ni is in progress.

Acknowledgment. We thank Shuwen Zhang for the preparation of the drawing, and Haiping Sun for the assistance in the HRTEM measurement. Y.L. is grateful for the research fellowships from the Alexander von Humboldt Foundation and the Singapore-MIT Alliance.

Supporting Information Available: Methods and detailed analyses of the crystalline orientation of the In and In_2O_3 nanoparticles. This material is available free of charge via the Internet at http://pubs.acs.org.

JA043969M